Synthetic model of the asymmetric $[Mn_3CaO_4]$ cubane core of the oxygen-evolving complex of photosystem II

Shreya Mukherjee[a], Jamie A. Stull[b], Junko Yano[c], Theocharis C. Stamatatos[a], Konstantina Pringouri[a], Troy A. Stich[b], Khalil A. Abboud[a], R. David Britt[b], Vittal K. Yachandra[c], and George Christou[a,1]

[a]Department of Chemistry, University of Florida, Gainesville, FL 32611; [b]Department of Chemistry, University of California at Davis, Davis, CA 95616; and [c]Physical Biosciences Division, Lawrence Berkeley National Laboratory, Berkeley, CA 94720

Edited by Harry B. Gray, California Institute of Technology, Pasadena, CA, and approved November 8, 2011 (received for review September 20, 2011)

The laboratory synthesis of the oxygen-evolving complex (OEC) of photosystem II has been the objective of synthetic chemists since the early 1970s. However, the absence of structural information on the OEC has hampered these efforts. Crystallographic reports on photosystem II that have been appearing at ever-improving resolution over the past ten years have finally provided invaluable structural information on the OEC and show that it comprises a $[Mn_3CaO_4]$ distorted cubane, to which is attached a fourth, external Mn atom, and the whole unit attached to polypeptides primarily by aspartate and glutamate carboxylate groups. Such a heterometallic Mn/Ca cubane with an additional metal attached to it has been unknown in the literature. This paper reports the laboratory synthesis of such an asymmetric cubane-containing compound with a bound external metal atom, $[Mn^{IV}_3Ca_2O_4(O_2CBu^t)_8(Bu^tCO_2H)_4]$ (1). All peripheral ligands are carboxylate or carboxylic acid groups. Variable-temperature magnetic susceptibility data have established 1 to possess an $S = 9/2$ ground state. EPR spectroscopy confirms this, and the Davies electron nuclear double resonance data reveal similar hyperfine couplings to those of other Mn^{IV} species, including the OEC S_2 state. Comparison of the X-ray absorption data with those for the OEC reveal 1 to possess structural parameters that make it a close structural model of the asymmetric-cubane OEC unit. This geometric and electronic structural correspondence opens up a new front in the multidisciplinary study of the properties and function of this important biological unit.

crystal structure | magnetic properties | spectroscopic properties

Photosystem II (PSII) is a multicomponent assembly of proteins and cofactors that is located in the thylakoid membrane of plants, algae, and cyanobacteria. It carries out the sunlight-driven oxidation of water to O_2, the generated protons driving ATP synthase and the electrons providing the reducing equivalents that ultimately lead to carbon dioxide fixation. The oxidation of water is an energetically demanding process, but the development approximately 2.7 billion years ago of a catalytic system capable of carrying it out efficiently made available as a raw material the vast quantities of water on the planet. The site of water oxidation to O_2 is the oxygen-evolving complex (OEC), and the determination of its structure has been the focus of much study by various biochemical and spectroscopic techniques. X-ray absorption spectroscopy (XAS), including extended X-ray absorption fine structure (EXAFS) and X-ray absorption near edge spectroscopy (XANES), have been invaluable tools in assessing possible metal topologies and distances between atoms that compose the OEC. These studies, along with those by EPR spectroscopy, have allowed for the description of Mn oxidation states at each of the S states (S_n, where $n = 0$–4) of the Kok cycle. Many groups have employed such spectroscopic data to guide their efforts toward the preparation of inorganic model complexes of the OEC, the goal being to improve our understanding of its structure and properties and ultimately to mimic its water oxidation function (1, 2). However, the absence of well-defined target structures has made this endeavor very challenging.

Following earlier X-ray studies at 3.8- (3) and 3.7-Å (4) resolution in 2001 and 2003, respectively, a 3.5-Å resolution structure on PSII from the cyanobacterium *Thermosynechococcus elongatus* in 2004 by Ferreira et al. (5) suggested a model for the OEC consisting of a $[Mn_3CaO_4]$ cubane with a fourth Mn attached to one of the cubane oxo ions and the resulting $[Mn_4CaO_4]$ primarily supported by monodentate carboxylate ligands provided by the residues of the D1 and CP43 polypeptides. Subsequent modifications to this proposal from modeling and theoretical studies included attachment of the fourth Mn via a fifth, external oxo-bridge to give a $[Mn_4CaO_5]$ core (6) or via both external and cubane oxide ions (7, 8). The moderate resolution of the crystallographic data and modification of the redox active Mn site by the X-ray beam (9) did not allow the precise structure of the Mn_4Ca cluster to be determined even when the resolution was improved to 2.9 Å (10). However, the recent structure at 1.9-Å resolution of PSII from *Thermosynechococcus vulcanus* by Umena et al. (11) has provided strong support for the suggestion by Barber and coworkers (5, 6) of a distorted cubane within the core, with the fourth Mn attached via both external and cubane oxo ions. Although biochemical studies had previously shown Ca to be essential for OEC activity, and X-ray spectroscopy had established the presence of an oxo-bridged Mn_4Ca heteronuclear cluster, these crystallographic data reenergized efforts to achieve the synthesis of the OEC in the laboratory. Several Mn/Ca compounds are now known (12–15), but there is only one complex that has approached the cubane moiety of the OEC structure (16). We here report the development of methodology for synthesizing in the absence of a protein milieu the $[Mn_3CaO_4]$ cubane with an external metal attached to it. The compound described here is a highly accurate synthetic model of the OEC metallocore, as gauged by comparisons of magnetic and spectroscopic data with those on the OEC, and opens up a front in the multidisciplinary study of the properties and function of this important biological site.

Author contributions: R.D.B., V.K.Y., and G.C. designed research; S.M., J.A.S., J.Y., T.C.S., K.P., K.A.A., and V.K.Y. performed research; S.M., J.A.S., J.Y., T.A.S., and K.A.A. analyzed data; and J.Y., R.D.B., and G.C. wrote the paper.

The authors declare no conflict of interest.

This article is a PNAS Direct Submission.

Data deposition: The crystallography, atomic coordinates, and structure factors have been deposited in the Cambridge Structural Database, Cambridge Crystallographic Data Centre, Cambridge CB2 1EZ, United Kingdom, http://www.ccdc.cam.ac.uk (CSD reference no. 844825).

[1]To whom correspondence should be addressed. E-mail: christou@chem.ufl.edu.

This article contains supporting information online at www.pnas.org/lookup/suppl/doi:10.1073/pnas.1115290109/-/DCSupplemental.

Results and Discussions

After extensive experimentation, the following procedure has been developed that takes advantage of readily available reagents. The reaction of $Mn(O_2CMe)_2 \cdot 4H_2O$, $Ca(NO_3)_2 \cdot 4H_2O$, and $NBu^n_4MnO_4$ in hot (80 °C) acetonitrile in the presence of an excess of pivalic acid gave a dark brown solution from which were subsequently isolated dark brown crystals of $[Mn_3Ca_2O_4(O_2CBu^t)_8(Bu^tCO_2H)_4]$ (**1**). The structure (Fig. 1 and *SI Appendix*, Table S1) consists of a $[Mn_3Ca(\mu_3\text{-}O^{2-})_4]$ cubane with an external Ca^{2+} attached at oxide O4 making the latter quadruply bridging (μ_4) and yielding a $[Mn_3Ca_2O_4]$ core. The +4 oxidation states of the three Mn ions and the nonprotonated nature of the bridging oxide ions were confirmed by Mn and O bond valence sum calculations, respectively (*SI Appendix*, Table S3). Ligation about the core is provided by eight pivalate groups bridging across Mn/Mn, Mn/Ca, and Ca/Ca pairs and four neutral pivalic acid groups bound in a monodentate fashion, two each on the Ca^{II} ions. The Mn···Ca separations [3.394(3)–3.454(3) Å] within the cubane of **1** agree with conclusions from Ca EXAFS studies on the OEC (approximately 3.4 Å) (17). The attachment of the external Ca to oxide O4 causes a significant lowering of the expected threefold symmetry of a $[Mn_3CaO_4]$ cubane, most notably in the Mn···Mn separations; Mn2···Mn3 [2.857(1) Å] is significantly longer than the others [2.730(1) and 2.757(1) Å] (Fig. 2*B*). This approximately 2.74- vs. 2.86-Å partition of Mn···Mn separations in a 2:1 ratio is consistent with high-resolution Mn EXAFS data on the OEC in the S_2 state, whose short Mn···Mn Fourier transform (FT) peaks can be fit to a 2:1 ratio of 2.73-:2.82-Å separations (18). The lowering of symmetry also has an effect, but to a lesser extent, on the Mn···Ca1 distances [3.4539(10) and 3.4178(10) vs. 3.3942(10) Å]. The remaining intermetallic separations and the Mn-O and Ca-O bond lengths are shown in Fig. 2 *A* and *B*. For comparison, the corresponding distances in the recent PSII structure (11) are shown in Fig. 2*C*: Differences between Figs. 2*A* and 2*C* are to be expected given the greater distance uncertainties in the crystal structure of a large PSII multicomponent assembly, structural perturbations caused by the polypeptide environment, and the fact that the OEC in the PSII crystal structure will be at the S_1 Kok state, or lower, and thus at least one of the cubane Mn atoms will be Mn^{III}, leading to slightly longer bond distances on average. Radiation modification of the Mn_4Ca center by about 25% can be estimated (19) from the X-ray dose reported by Umena and coworkers (11), which will lead to longer Mn-ligand, Mn-Mn, and Mn-Ca distances.

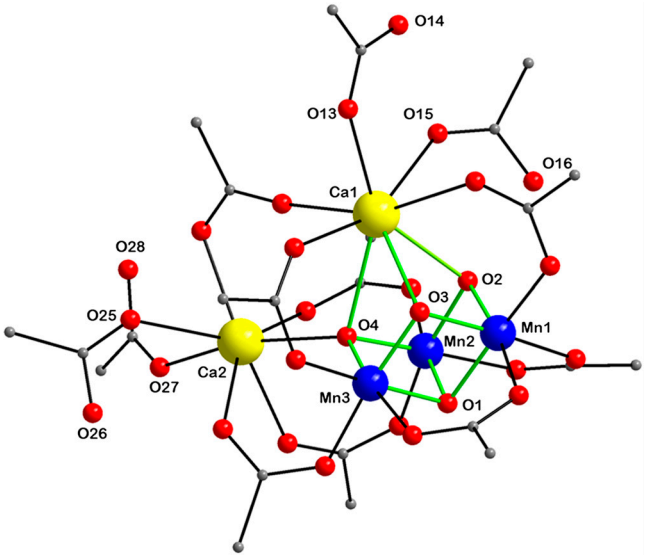

Fig. 1. Crystallographic results for complex **1**. The structure of **1**, with the pivalate CH_3 groups omitted for clarity. Color scheme: Mn^{IV}, blue; Ca^{II}, yellow; O, red; C, gray; the $[Mn_3CaO_4]$ cubane is emphasized with green bonds.

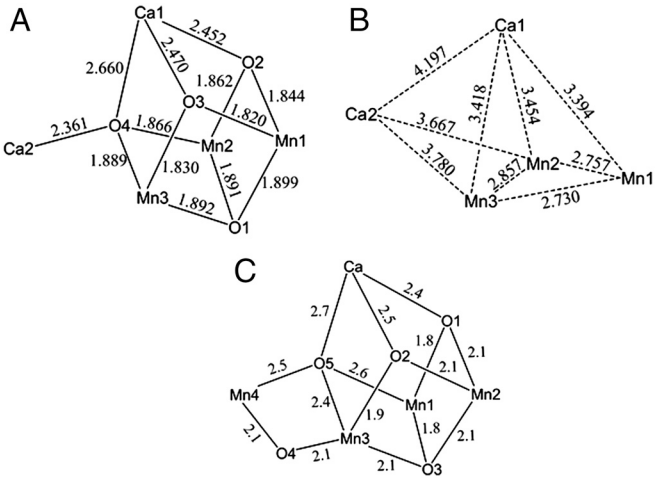

Fig. 2. (*A*) Bond distances in **1**; the estimated standard deviations are 0.003 Å. (*B*) Metal-metal separations in **1**; the estimated standard deviations are 0.001 Å. (*C*) Bond distances in the 1.9 Å PSII structure by Umena et al. (11); atom labels are as in ref. 11.

Mn and Ca XAS. Mn and Ca XAS have provided important insights into the nature of the OEC (20, 21). The formal oxidation states of the S_0, S_1, and S_2 states are generally accepted as $Mn^{III}_3Mn^{IV}$, $Mn^{III}_2Mn^{IV}_2$, and $Mn^{III}Mn^{IV}_3$, respectively. The proposed formal oxidation states for the S_3 state are Mn_4^{IV}, or $Mn^{III}Mn^{IV}_3$ with the other oxidative equivalent delocalized onto the O ligand atoms. Fig. 3 compares the Mn XANES spectra of the OEC in the S_0–S_3 states with the spectrum of the Mn_3Ca_2 complex **1**. The formal oxidation state of **1** is $Mn^{IV}_3Ca_2$, and its edge position falls between the S_2 and S_3 states. Interestingly, the shape of the edge of complex **1** is similar to that seen for the OEC. Of the many multinuclear Mn complexes that have been synthesized, this kind of similarity with the OEC has been observed previously only for the distorted Mn_4 cubane-like complexes that are $Mn^{III}_4Mn^{IV}$ (22) and which, like complex **1**, also have mostly nonaromatic O-based ligands.

Mn EXAFS studies of the OEC in the S_1 and S_2 states have established the presence of two Mn···Mn distances at approximately 2.7 Å and one Mn···Mn distance of approximately 2.8 Å, characteristic of di-μ-oxide-bridged Mn_2 pairs with mostly O-based ligation at 1.8–2.0 Å. The Mn EXAFS also shows a longer distance interaction, assigned to one Mn···Mn distance at 3.3 Å,

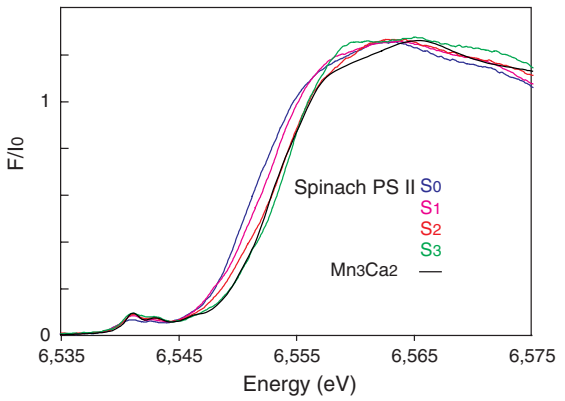

Fig. 3. Mn XANES from spinach PSII in the S_0, S_1, S_2, and S_3 states compared with the spectrum from the $Mn^{IV}_3Ca_2$ complex **1**.

and Mn···Ca at approximately 3.4 Å. Further support for including a Mn···Ca at approximately 3.4 Å comes from Sr EXAFS studies on PSII in which the calcium was replaced with strontium. In that work, four Mn···Sr(Ca) distances in the 3.4–3.9 Å range were detected (23). These Mn···Mn and Mn···Ca distances are known to change during the S-state cycle. Fig. 4 shows the comparison of the Mn and Ca EXAFS of the OEC in the S_1 state with Mn_3Ca_2 complex **1**. The comparison of the Mn EXAFS in Fig. 4*A* shows that there are similarities in the beat pattern but there are many differences in the phase, frequencies, and intensity of the spectral features. The corresponding FT in Fig. 4*B* shows that there is substantial similarity in the features, except for the difference in the intensity of the FT peak at approximately 1.8–2.0 Å—i.e., from Mn-ligand distances. The similarity in the FT peak at 2.7–2.8 Å is due to the presence of three Mn···Mn distances at 2.7–2.8 Å in both the OEC and complex **1**. The FT peak at approximately 3.3 Å is also similar between the OEC and **1** because of the presence of Mn···Mn/Ca distances of approximately 3.3 Å in both systems. The differences in the spectra are not surprising because of the presence of the extra (external) Ca atom in Mn_3Ca_2 that is not present in the OEC (Mn_4Ca). Fig. 4 *C* and *D* shows the Ca EXAFS and the FTs of the OEC in the S_1 state compared with that from **1**. The Ca EXAFS spectra in Fig. 4*C* show, just as in the Mn EXAFS, that there are similarities between the $[Mn_3Ca_2]$ cluster and the OEC; however, there are still differences in frequency and intensity. The FTs show that the OEC and **1** both have similar Ca···Mn distances including the first FT peak from Ca-O distances and the second FT peak at approximately 3.3 Å from Ca···Mn distances. The differences are again not surprising because of the presence of the extra Ca atom in the complex. Overall, the similarities in both the Mn and Ca EXAFS and FTs show that complex **1** has many of the features, especially the Mn···Mn and Mn···Ca distances, that are present in the OEC. This degree of similarity in the spectra between the OEC and a model complex is unique and has not been seen in comparisons with myriad Mn complexes that have been synthesized to date. Fits of the Mn and Ca EXAFS data of **1** to the crystal structure parameters are provided in *SI Appendix*.

Magnetic Susceptibility Studies. To determine the ground state spin (S) of **1**, magnetic susceptibility (χ_M) data were collected for a microcrystalline sample in the 5.0–300 K range in a 0.10-T field and are plotted as $\chi_M T$ vs. T in Fig. 5*A*. The increasing $\chi_M T$ with decreasing T indicates dominant ferromagnetic coupling in the molecule, and the low-temperature data indicate an $S = 9/2$ ground state. To obtain the Mn···Mn exchange interactions, the data were fit to an isosceles model employing two exchange parameters J and J', where J' is the unique Mn2···Mn3 interaction. The Heisenberg–Dirac–van Vleck spin Hamiltonian ($\mathscr{H}$) for an isosceles triangle of isotropic Mn^{4+} ($t_{2g}{}^3$) ions is given by

$$\mathscr{H} = -2J(\hat{S}_1 \cdot \hat{S}_2 + \hat{S}_1 \cdot \hat{S}_3) - 2J'(\hat{S}_2 \cdot \hat{S}_3), \quad [1]$$

where the subscripts refer to the Mn atom numbering of Fig. 2 and $S_1 = S_2 = S_3 = 3/2$ for Mn^{IV}. The eigenvalues of this spin Hamiltonian are given by

$$E|S_T,S_A\rangle = -J[S_T(S_T+1) - S_A(S_A+1)] - J'[S_A(S_A+1)] \quad [2]$$

obtained analytically by using the Kambe method (24) with the substitutions $\hat{S}_A = \hat{S}_2 + \hat{S}_3$ and $\hat{S}_T = \hat{S}_1 + \hat{S}_A$, where $\hat{S}_T$ is the to-

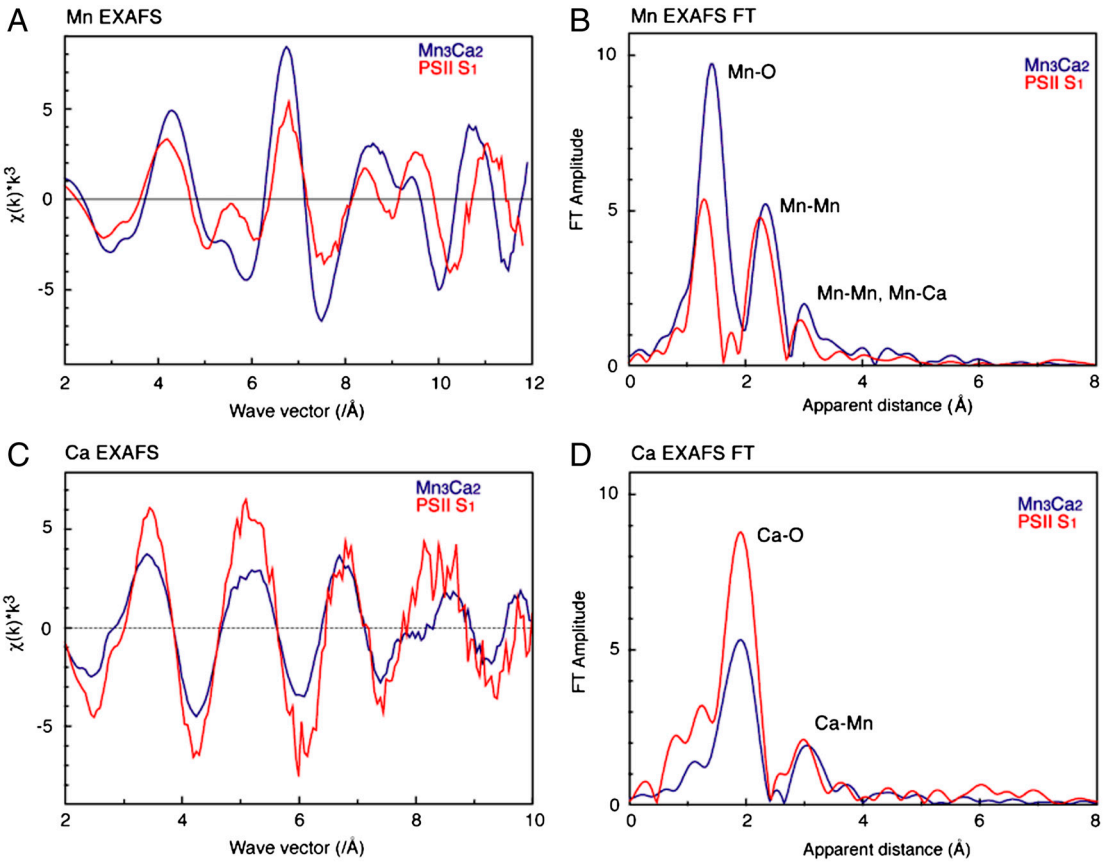

Fig. 4. (*A* and *B*) The Mn EXAFS and the Fourier transforms of the OEC in the S_1 state, compared with complex **1**. (*C* and *D*) The Ca EXAFS and the Fourier transforms of the OEC in the S_1 state compared with complex **1**.

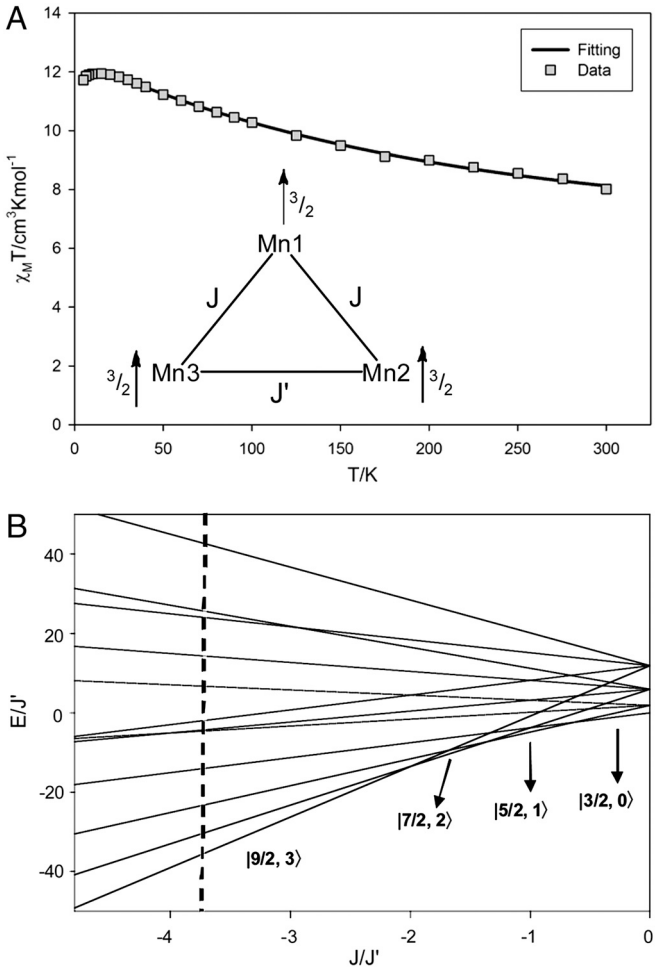

Fig. 5. Results of the magnetism studies on complex **1**. (*A*) $\chi_M T$ vs. T data and fit; see the text for the fit parameters. The *Inset* shows the exchange coupling model employed and the spin alignments in the $S_T = 9/2$ ground state. (*B*) Plot of S_T energies vs. the J/J' ratio, showing the change in ground state. The dashed line corresponds to the experimentally determined J/J' ratio of −3.75 for complex **1**.

tal spin of the molecule and $E|S_T,S_A\rangle$ is the energy of state S_T obtained from a given S_A. Complex **1** has twelve S_T states with values in the range $S_T = 1/2$–$9/2$. The S_T values and their energies were input into the van Vleck equation (25) to derive the theoretical $\chi_M T$ vs. T equation, which was used to fit the experimental data (solid line in Fig. 5*A*) to give $J = +40.5(1)$ cm^{-1}, $J' = -10.8(7)$ cm^{-1}, and $g = 1.960(2)$, with a contribution from temperature-independent paramagnetism held constant at 300×10^{-6} cm^3 mol^{-1}. The molecule has a $|9/2,3\rangle$ ground state, with all Mn^{IV} spins aligned parallel (Fig. 5*A*, *Inset*) and a $|7/2,2\rangle$ first excited state 56.7 cm^{-1} above the ground state. $J > 0$ and $J' < 0$ represent competing interactions within a triangular unit, but the $|J| \gg |J'|$ situation overcomes the antiferromagnetic J' leading to parallel spin alignments.

Such strong ferromagnetic coupling between Mn^{IV}Mn^{IV} pairs is extremely rare and is assigned to the acute Mn1-O-Mn2 and Mn1-O-Mn3 angles [92.11(11)–96.81(12)°], with slightly greater Mn2-O-Mn3 angles [98.08(12)°, 99.05(12)°] caused by the external Ca making J' antiferromagnetic. This sensitivity to small angle changes at monatomic bridges is well recognized in the 90–100° range (26). Because the exchange couplings are competing, the S_T energies as a function of the J/J' ratio were calculated and are presented in Fig. 5*B* for $J > 0$ and $J' < 0$. The $J/J' = -3.75$ for **1** is well within the $S_T = 9/2$ ground state region, but three other states with progressively smaller S_T values would become the ground state as the J/J' ratio decreases, which would require relatively small angle changes. This decrease would lead ultimately to the $|3/2,0\rangle$ ground state when $|J| \ll |J'|$ and the ferromagnetic J is frustrated. Fig. 5*B* thus reveals how accessible alternative ground states could be with relatively small structural perturbations.

EPR Spectroscopy. The low-temperature EPR spectrum of complex **1** is complicated because of the zero-field splitting (ZFS) of the five Kramers doublets of the $S_T = 9/2$ spin system (Fig. 6). The effective ZFS constants ($|D| = 0.068$ cm^{-1}, $E = 0.0052$ cm^{-1}) were determined by simultaneously fitting spectra acquired at the X (9.375 GHz) and Q bands (34.188 GHz). Additional splittings from the hyperfine interactions (HFI) of the three ^{55}Mn ($I = 5/2$) nuclei are obscured in the inhomogeneously broadened EPR line. These ^{55}Mn HFI were probed by using Davies electron nuclear double resonance (ENDOR), and the spectrum collected at 1,144.2 mT (*SI Appendix*, Fig. S5) reveals eight peaks in the 0–200 MHz frequency range. The relative peak intensities change as the field is varied because of each experiment being resonant to a different degree with some of the overlapping EPR transitions (see *SI Appendix*, Fig. S5). For each ^{55}Mn nucleus, a set of two ENDOR peaks centered at $A * m_S$ and split by twice the Larmor frequency [e.g., $2 * \nu_L(^{55}\text{Mn}) = 26.2$ MHz at 1,200 mT] is expected. Each of these peaks will be further split into sextets because of the nuclear quadrupole interaction (NQI). Although these individual transitions are unlikely to be resolved, they will manifest as an m_S-dependent broadening of each ENDOR line (27). To model this behavior in our simulations, NQI parameters $P_{||}$ and η were respectively set to 2.5 MHz and 0.2, intermediate of values found for Mn^{IV} centers in other exchange-coupled clusters (14, 28). To further simplify the analysis of the ENDOR spectrum, the isosceles triangle model (above) was applied. Two classes of hyperfine-coupled Mn centers were considered, and the best fit of all the field-dependent ENDOR data yielded the following set of effective hyperfine parameters: for the two equivalent Mn nuclei, $A_{2,3} = [61,61,63]$ MHz and $A_1 = [61,61,57]$

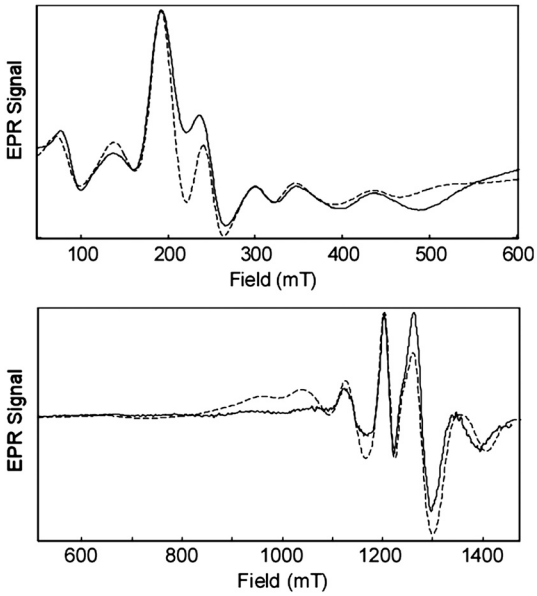

Fig. 6. Continuous wave EPR spectra at the X band (9.3752 GHz) and Q band (34.1877 GHz; derivative) of complex **1**. All spectra were acquired at 5 K. Simulations (dashed line) of data generated by using the following parameters: spin $S = 9/2$; $g = 1.975$; zero-field splitting $|D| = 0.068$ cm^{-1}, $E = 0.0052$ cm^{-1}; linewidth 16 mT.

MHz for the unique Mn center (numbering scheme the same as that in Fig. 1).

Because the total effective spin ($S_T = 9/2$) of **1** is different from that of the isolated ions (S of Mn^{IV} is 3/2), the observed HFI must be scaled by an appropriate projection factor. With $J \gg D$ (i.e., strong exchange coupling limit), the projection factors for each Mn^{IV} ion are simply 1/3 (28). As a result, the magnitude of the site-specific HFI are $a_{2,3} = [183,183,189]$ MHz and $a_1 = [183,183,171]$ MHz. These Mn^{IV} hyperfine values—in particular, the low value of the hyperfine anisotropy—compare well to those of other Mn^{IV}-containing synthetic and biological systems (*SI Appendix*, Table S4), such as the S_2 state of the OEC (29). The slightly smaller values for the isotropic part of the hyperfine could be due to spin-polarization effects (30) and strong covalent bonding with the carboxylates that complete the coordination sphere of the Mn^{IV} ions. This covalency would draw spin density away from the Mn ions, leading to reduced metal hyperfine interactions.

Conclusions

Inspired by recent X-ray crystal structures of PSII showing the OEC to be composed of a $[Mn_4CaO_x]$ cluster primarily ligated to protein carboxylate groups, we have synthesized complex **1**, an asymmetric $[Mn_3CaO_4]$ carboxylate cubane with an additional Ca ion attached in place of the fourth, external Mn ion. The simple ligand sphere composed of carboxylate groups shows that this low-nuclearity, high-valent, heterometallic cubane unit does not owe its existence and stabilization within PSII to the environmental effects and restrictions of a polypeptide tertiary structure. In addition, the structural asymmetry of **1** leads to interatomic distances that are very similar to those determined for the OEC by EXAFS spectroscopy, and in general the XANES and EXAFS data have demonstrated a high degree of structural similarity between **1** and the OEC. These comparisons establish **1** as a close structural model of the overall topology of the OEC. Of course, the extent to which the Mn_3CaO_4 cubane core of the OEC is more greatly distorted by its polypeptide environment is still an open question. Furthermore, neutral pivalic acid groups attached to the cubane and external Ca atoms are intriguingly reminiscent of the terminal solvent-derived ligands attached to the cubane Ca and external Mn atom seen in the recent 1.9-Å structure of the OEC (11).

The above points make **1** distinctly different from the recently reported $[Mn_3CaO_4(O_2CMe)_3L]$ (**2**) complex (16), where L is an O_3, N_3 hexadentate platform group providing pyridyl and alkoxo ligands to each of the three Mn^{IV} ions. Complex **2** contains a $[Mn_3CaO_4]$ cubane without an external metal ion, and as a result it closely approaches threefold symmetry with Mn···Mn and Ca···Mn distances in the 2.8301(7)–2.8385(7) and 3.2245(9)–3.2376(9) Å ranges, respectively. The presence of the diamagnetic external Ca in **1** is thus advantageous in providing the low symmetry structure analogous to the OEC and also allowing the intrinsic magnetic properties of the distorted cubane to be characterized in the absence of a complicating external paramagnetic ion. This simplification is of critical importance to our efforts to disentangle the magnetic interactions within the OEC that give rise to rich magnetic resonance behavior. The magnetic study of **1** reveals an $S_T = 9/2$ ground state from strong ferromagnetic exchange interactions ($J \approx 40$ cm^{-1}) that are rare in the inorganic literature but are assignable in the present case to the acute Mn-O-Mn angles characteristic of a cubane structure. This finding supports similarly strong ferromagnetic $Mn^{IV}Mn^{IV}$ coupling ($J \approx 30$ cm^{-1}) recently invoked to explain the ^{55}Mn ENDOR spectra of the OEC in the S_2 state (30). In addition, Fig. 5 shows that small changes to the relative magnitude of J and J', as could arise from small structural perturbations and/or differing protonation levels of one or more bridging O atoms, can readily yield a different ground state, which could be useful to probe additional S states of the Kok cycle. For example, it is well known there are two EPR signals associated with the OEC in PSII when poised in the S_2 ($Mn^{III}Mn^{IV}{}_3$) state (31): the "multiline signal" that is associated with an $S = 1/2$ ground state and the less well-understood $g = 4.1$ signal that corresponds to an $S = 5/2$ ground state (32). One possible spin configuration that could give rise to an $S = 5/2$ state is the antiferromagnetic coupling between the $[Mn^{IV}{}_3CaO_4]$ ($S = 9/2$) cubane and an external Mn^{III} ($S = 2$) yielding an $S = 5/2$ cluster. In addition, recent EPR studies suggest an $S = 3$ ground state for the S_3 state of the OEC (33), which could arise from the $[Mn^{IV}{}_3CaO_4]$ cubane antiferromagnetically coupled to an external Mn^{IV} ($S = 3/2$). Also, because Mn-centered oxidation is purported not to occur during the S_3 to S_4 transition (34), further study of **1** and its analogs may provide insights into the structure of this elusive PSII intermediate. Thus, complex **1** approaches both the geometric and electronic structure of the OEC and provides a foundation for ongoing efforts to extend this work to additional relevant models of the OEC. We are currently exploring ligand variation in **1** to impose structural perturbations that might also alter the ground state by altering the J/J' ratio, the replacement of the external Ca with Mn, and assessing reactivity as a basis for developing biomimetic water oxidation activity (35–39). The attainment of **1** is an important breakthrough that provides a valuable foundation for future work in various directions and should permit a deeper level of insights into the nature and mode of action of this crucial biological site.

Materials and Methods

Synthesis of Complex 1. All manipulations were carried out under aerobic conditions by using chemicals as received, unless otherwise stated. $NBu^n{}_4MnO_4$ was prepared as described elsewhere (40). Infrared spectra were recorded in the solid state (KBr pellets) on a Nicolet Nexus 670 FTIR spectrometer in the 400–4,000 cm^{-1} range. Elemental analysis (C, H, and N) was performed by the in-house facilities of the University of Florida, Chemistry Department.

$[Mn_3Ca_2O_4(O_2CBu^t)_8(HO_2CBu^t)_4]$ (1). $Mn(O_2CCH_3)_2 \cdot 4H_2O$ (0.5 mmol, 0.12 g) was dissolved in hot acetonitrile (25 mL), and the resulting pink solution was treated with pivalic acid (16.4 mmol, 1.88 mL) and $Ca(NO_3)_2 \cdot 4H_2O$ (0.50 mmol, 0.12 g), which caused the color to change to deep red. The solution was stirred at 80 °C for 15 min, and during this period solid $NBu^n{}_4MnO_4$ (4.0 mmol, 1.44 g) was added in small portions. The resulting dark brown solution was allowed to cool to room temperature and filtered, and the filtrate left undisturbed. After 4 d, X-ray quality dark brown plate like crystals of **1** had formed and were collected by filtration and dried under vacuum. Yield: 48%. Elemental analysis (%) calculated for $C_{60}H_{112}O_{28}Mn_3Ca_2$ (**1**): C 47.21, H 7.39; found: C 47.04, H 7.59.

Other Spectroscopic Characterizations. The X-band and Q-band EPR data were collected at the CalEPR center at the University of California at Davis. Ca X-ray absorption spectra were measured at beamlines 10.3.2 at the Advanced Light Source, Berkeley, and 4-3 of the Stanford Synchrotron Radiation Lightsource (SSRL). Mn X-ray absorption spectra were collected at the SSRL beamline 7-3 (see *SI Appendix, Materials and Methods* for more details on the experimental setup and simulations).

ACKNOWLEDGMENTS. Stefan Stoll (University of Washington) is acknowledged for assistance with EPR simulations. This work was supported by the University of Florida, the National Institutes of Health (GM 55302 to V.K.Y.), and the Department of Energy (DOE), Director, Office of Science, Office of Basic Energy Sciences, Chemical Sciences, Geosciences, and Biosciences Division, under Contract DE-AC02-05CH11231 (to J.Y. and V.K.Y.) and Contracts DE-FG02-10ER16150 and DE-SC000-7203 (to R.D.B.). Portions of this research were carried out at Stanford Synchrotron Radiation Lightsource, Stanford, and the Advanced Light Source, Berkeley, funded by DOE, Director, Office of Science, Office of Basic Energy Sciences. The Stanford Synchrotron Radiation Lightsource Structural Molecular Biology Program is supported by the DOE, Office of Biological and Environmental Research and by the National Institutes of Health, National Center for Research Resources. The EPR spectrometers used in this study are part of the CalEPR center and were funded by the University of California, Davis and National Institutes of Health (S10-RR02075).

1. Batista VS, Sproviero EM, Gascon JA, McEvoy JP, Brudvig GW (2008) Computational studies of the O_2-evolving complex of photosystem II and biomimetic oxo manganese complexes. *Coord Chem Rev* 252:395–415.
2. Mukhopadhyay S, Mandal SK, Bhaduri S, Armstrong WH (2004) Manganese clusters with relevance to photosystem II. *Chem Rev* 104:3981–4026.
3. Zouni A, et al. (2001) Crystal structure of photosystem II from Synechococcus elongatus at 3.8 angstrom resolution. *Nature* 409:739–743.
4. Kamiya N, Shen JR (2003) Crystal structure of oxygen-evolving photosystem II from Thermosynechococcus vulcanus at 3.7-angstrom resolution. *Proc Natl Acad Sci USA* 100:98–103.
5. Ferreira KN, Iverson TM, Maghlaoui K, Barber J, Iwata S (2004) Architecture of the photosynthetic oxygen-evolving center. *Science* 303:1831–1838.
6. Barber J, Murray JW (2008) Revealing the structure of the Mn-cluster of photosystem II by X-ray crystallography. *Coord Chem Rev* 252:233–243.
7. Dau H, Grundmeier A, Loja P, Haumann M (2008) On the structure of the manganese complex of photosystem II: Extended-range EXAFS data and specific atomic-resolution models for four S-states. *Philos Trans R Soc Lond B* 363:1237–1243.
8. Siegbahn PEM (2008) A structure-consistent mechanism for dioxygen formation in photosystem II. *Chemistry* 14:8290–8302.
9. Yano J, et al. (2005) X-ray damage to the Mn4Ca complex in single crystals of photosystem II: A case study for metalloprotein crystallography. *Proc Natl Acad Sci USA* 102:12047–12052.
10. Guskov A, et al. (2009) Cyanobacterial photosystem II at 2.9-angstrom resolution and the role of quinones, lipids, channels and chloride. *Nat Struct Mol Biol* 16:334–342.
11. Umena Y, Kawakami K, Shen JR, Kamiya N (2011) Crystal structure of oxygen-evolving photosystem II at a resolution of 1.9 angstrom. *Nature* 473:55–U65.
12. Hewitt IJ, et al. (2006) A series of new structural models for the OEC in photosystem II. *Chem Commun* 2650–2652.
13. Jerzykiewicz LB, Utko J, Duczmal M, Sobota P (2007) Syntheses, structure, and properties of a manganese-calcium cluster containing a Mn_4Ca_2 core. *Dalton Trans* 28:825–826.
14. Kotzabasaki V, Siczek M, Lis T, Milios CJ (2011) The first heterometallic Mn-Ca cluster containing exclusively Mn(III) centers. *Inorg Chem Commun* 14:213–216.
15. Mishra A, Wernsdorfer W, Abboud KA, Christou G (2005) The first high oxidation state manganese-calcium cluster: Relevance to the water oxidizing complex of photosynthesis. *Chem Commun* 54–56.
16. Kanady S, Tsui E, Day M, Agapie T (2011) A synthetic model of the Mn3Ca subsite of the oxygen-evolving complex in photosystem II. *Science* 333:733–736.
17. Cinco RM, et al. (2002) Calcium EXAFS establishes the Mn-Ca cluster in the oxygen-evolving complex of photosystem II. *Biochemistry* 41:12928–12933.
18. Yano J, et al. (2005) High-resolution Mn EXAFS of the oxygen-evolving complex in photosystem II: Structural implications for the Mn_4Ca cluster. *J Am Chem Soc* 127:14974–14975.
19. Yano J, et al. (2005) X-ray damage to the Mn_4Ca complex in single crystals of photosystem II: A case study for metalloprotein crystallography. *Proc Natl Acad Sci USA* 102:12047–12052.
20. Yano J, et al. (2006) Where water is oxidized to dioxygen: Structure of the photosynthetic Mn_4Ca cluster. *Science* 314:821–825.
21. Yano J, Yachandra VK (2008) Where water is oxidized to dioxygen: Structure of the photosynthetic Mn_4Ca cluster from X-ray spectroscopy. *Inorg Chem* 47:1711–1726.
22. Cinco RM, et al. (1999) Comparison of the manganese cluster in oxygen-evolving photosystem II with distorted cubane manganese compounds through X-ray absorption spectroscopy. *Inorg Chem* 38:5988–5998.
23. Pushkar YL, Yano J, Sauer K, Boussac A, Yachandra VK (2008) Structural changes in the Mn_4Ca cluster and the mechanism of photosynthetic water splitting. *Proc Natl Acad Sci USA* 105:1879–1884.
24. Kambe K (1950) On the paramagnetic susceptibilities of some polynuclear complex salts. *J Phys Soc Jpn* 5:48–51.
25. Vleck JHV (1932) *The Theory of Electric and Magnetic Susceptibilities* (Oxford Univ Press, London).
26. Kahn O (1993) *Molecular Magnetism* (VCH, New York).
27. Sturgeon BE, Ball JA, Randall DW, Britt RD (1994) ^{55}Mn electron-spin echo ENDOR of Mn^{2+} complexes. *J Phys Chem* 98:12871–12883.
28. Randall DW, et al. (1995) ^{55}Mn ESE-Endor of a mixed-valence Mn(III)Mn(IV) complex—Comparison with the Mn cluster of the photosynthetic oxygen-evolving complex. *J Am Chem Soc* 117:11780–11789.
29. Cox N, et al. (2011) Effect of Ca^{2+}/Sr^{2+} substitution on the electronic structure of the oxygen-evolving complex of photosystem II: A combined multifrequency EPR, ^{55}Mn-ENDOR, and DFT study of the S_2 state. *J Am Chem Soc* 133:3635–3648.
30. Munzarova ML, Kubacek P, Kaupp M (2000) Mechanisms of EPR hyperfine coupling in transition metal complexes. *J Am Chem Soc* 122:11900–11913.
31. Dismukes GC, Siderer Y (1980) EPR spectroscopic observations of a manganese center associated with water oxidation in spinach-chloroplasts. *FEBS Lett* 121:78–80.
32. Haddy A, Lakshmi KV, Brudvig GW, Frank HA (2004) Q-band EPR of the S_2 state of photosystem II confirms an $S = 5/2$ origin of the X-band $g = 4.1$ signal. *Biophys J* 87:2885–2896.
33. Boussac A, Sugiura M, Rutherford AW, Dorlet P (2009) Complete EPR spectrum of the S_3-state of the oxygen-evolving photosystem II. *J Am Chem Soc* 131:5050–5051.
34. Haumann M, et al. (2005) Photosynthetic O_2 formation tracked by time-resolved X-ray experiments. *Science* 310:1019–1021.
35. Brudvig GW (2008) Water oxidation chemistry of photosystem II. *Philos Trans R Soc Lond B* 363:1211–1218.
36. Li G, et al. (2009) Deposition of an oxomanganese water oxidation catalyst on TiO_2 nanoparticles: Computational modeling, assembly and characterization. *Energy Environ Sci* 2:230–238.
37. Hocking RK, et al. (2011) Water-oxidation catalysis by manganese in a geochemical-like cycle. *Nat Chem* 3:461–466.
38. Jiao F, Frei H (2010) Nanostructured manganese oxide clusters supported on mesoporous silica as efficient oxygen-evolving catalysts. *Chem Commun* 46:2920–2922.
39. Najafpour MM, Ehrenberg T, Wiechen M, Kurz P (2010) Calcium manganese(III) oxides ($CaMn_2O_4 \cdot xH_2O$) as biomimetic oxygen-evolving catalysts. *Angew Chem Int Ed* 49:2233–2237.
40. Sala T, Sargent MV (1978) Tetrabutylammonium permanganate—Efficient oxidant for organic substrates. *J Chem Soc Chem Commun* 253–254.